

In-human testing of a non-invasive continuous low-energy microwave glucose sensor with advanced machine learning capabilities

Nazli Kazemi^{a,*}, Mohammad Abdolrazzaghi^b, Peter E.Light^c and Petr Musilek^d

^aElectrical and Computer Engineering, University of Alberta, 116 st, Edmonton, T6G 2R3, AB, Canada

^bUniversity of Toronto, 10 King's College Rd, Toronto, M5S 3G4, ON, Canada

^cFaculty of Medicine and Dentistry Department of Pharmacology, Alberta Diabetes Institute, University of Alberta, 112 St., Edmonton, T6G 2R3, AB, Canada

^dElectrical and Computer Engineering, University of Alberta, 116 st., Edmonton, T6G 2R3, AB, Canada

^dApplied Cybernetics, University of Hradec Králové, Rokitanského 62/26, Hradec Králové, 500 03, Czechia, Czech Republic

ARTICLE INFO

Keywords:

Time series neural network
microwave sensor
glucose
anomaly detection
machine learning
LSTM


ABSTRACT

Continuous glucose monitoring schemes that avoid finger pricking are of utmost importance to enhance the comfort and lifestyle of diabetic patients. To this aim, we propose a microwave planar sensing platform as a potent sensing technology that extends its applications to biomedical analytes. In this paper, a compact planar resonator-based sensor is introduced for noncontact sensing of glucose. Furthermore, *in vivo* and *in-vitro* tests using a microfluidic channel system and in clinical trial settings demonstrate its reliable operation. The proposed sensor offers real-time response and a high linear correlation ($R^2 \sim 0.913$) between the measured sensor response and the blood glucose level (GL). The sensor is also enhanced with machine learning to predict the variation of body glucose levels for non-diabetic and diabetic patients. This addition is instrumental in triggering preemptive measures in cases of unusual glucose level trends. In addition, it allows for the detection of common artifacts of the sensor as anomalies so that they can be removed from the measured data. The proposed system is designed to noninvasively monitor interstitial glucose levels in humans, introducing the opportunity to create a customized wearable apparatus with the ability to learn.

1. Introduction

Wearable electronics are designed to monitor body signals and enable real-time and continuous sensing without interrupting or limiting the user's motion (Bariya et al., 2018; Gao et al., 2016; Park et al., 2018; Nyein et al., 2021; Barrett et al., 2014). Recently, a wide range of wearable electronics have been introduced to monitor physiological activities and detect their changes to diagnose diseases (Zheng et al., 2005; Chen et al., 2014; Farandos et al., 2015; Pankratov et al., 2016). As a growing concern, diabetes mellitus is currently a chronic disease. The number of patients is on the rise, with an estimated 537 million people suffering from the disease in 2021. This translates into an increase of 190 % since 1980 (Wild et al., 2004). These patients are also at risk of developing complications such as kidney disease, blindness, stroke, and cardiovascular problems. They are advised to monitor their blood GL periodically and to administer insulin via injection in the event of excessive GL. Clearly, continuous monitoring of GL is advantageous to simplify its management and reduce associated risks (Lee et al., 2021; Zou et al., 2023; Agustini et al., 2017).

Conventional methods include pricking a finger to sample capillary blood that is used on a test strip containing an electrochemical sensor (Chen et al., 2019; Lee et al., 2016). This intrusive method allows for only periodic blood glucose measurements and can cause discomfort for many, including children and the elderly, with non-negligible consumable strip costs. Neither this method keeps the history of past events due to the nature of the single-time measurement. The continuous monitoring devices such as Freestyle Libre and Dexcom G6, besides being costly, are limited by their accuracy when the glucose level surges rapidly due to either high sugar intake or missed insulin intake, wherein some discrepancy could be observed (e.g. Freestyle Libre could relay 200 mg/dL as opposed to more accurate value of 150 mg/dL read by AccuChek). Several noninvasive techniques have been introduced in the literature (Lee

 nazli@ualberta.ca (N. Kazemi); abdolra3@ece.utoronto.ca (M. Abdolrazzaghi); plight@ualberta.ca (P. E.Light); pmusilek@ualberta.ca (P. Musilek)

ORCID(s):

et al., 2017; Chen et al., 2017; Pu et al., 2021) including electrochemical and optical regimes. In the former, the skin impedance measurement (Pleus et al., 2021; Kim et al., 2018; Nyein et al., 2021; Gao et al., 2016) is used to predict the GL of the body, since glucose diffuses to the skin surface. Unfortunately, patients found that these devices had erroneous readouts and caused skin burns and irritation. Optical methods such as Raman spectroscopy, infrared absorption, and optical coherence tomography, report unreliable Clarke error grid analysis (Wentholt et al., 2006). Other techniques offer portable instrumentation, including contact lens as an electrochemical biosensor (Keum et al., 2020; Liao et al., 2011; Badugu et al., 2005; Kim et al., 2017; Park et al., 2018; Kownacka et al., 2018) and occlusion spectroscopy (Amir et al., 2007). However, most of these techniques have high uncertainties ($\geq \pm 30 \text{ mg/dL}$) in detecting GL suitable for human body.

Electromagnetic sensing (EM) is an emerging technology that uses the propagation of electromagnetic waves and their interaction with the material under test (MUT). Microwave sensors have been used to detect glucose content in both *in vivo* (Srichan et al., 2022; Caduff et al., 2003; Kim et al., 2015) and *ex vivo* (Yilmaz et al., 2014; Gorst et al., 2021; Kazemi and Musilek, 2023, 2022) configurations, allowing non-invasive monitoring (Omer et al., 2020; Hanna et al., 2020; Abdolrazzagli et al., 2021). Illumination of an object with microwave radiation results in the transmission and reflection of EM waves that are used to characterize the MUT (Piekarz et al., 2020; Guliy et al., 2019; Abdolrazzagli et al., 2018; Ebrahimi et al., 2021; Azimi Dijvejin et al., 2022; Rawat et al., 2017). The relationship between the input and output of the sensor is expressed in terms of complex quantities called scattering parameters. Because the behavior of these waves depends on the dielectric properties of the host medium, these sensors can be used to detect any variation within the medium. More precisely, the amplitude and phase of the sensor response (either reflection/transmission) are affected by the medium and hold information about the composition of the MUT. Because all components of a composite environment might contribute to a change in the dielectric property at certain frequency, it is always necessary to investigate the dependence of the sensor response on each component individually. In the case of glucose monitoring, there is good coherence between the sensor response and the glucose content only, regardless of any peripheral ingredients. This is due to the major contribution of glucose (Hanna et al., 2020; Choi et al., 2015; Baghelani et al., 2020). Microwave sensors inspired by the inclusion of metamaterials are compact and have a low-profile design (Abdolrazzagli and Daneshmand, 2020; Albishi et al., 2020; Mohammadi et al., 2019). Their non-contact sensing makes them popular in many applications, while their low cost facilitates mass production. Highly sensitive elements, including split-ring resonators (SRR) and patches, are repeatedly used in numerous sensors because they offer localized regions sensitive to capacitive variations in the environment. In this regard, the sensitivity of separately used microwave sensors is poor. In contrast, when two or more similar or different designs are coupled, their sensitivity is significantly enhanced, and their size is subsequently also reduced (Omer et al., 2020). This technique is used when a patch resonator is tightly coupled with an SRR to obtain a miniaturized ultra-high-sensitivity sensor.

The proposed sensor is used to continuously measure glucose content for both microfluidic (μF) channel configuration and human trials. The continuous nature of glucose measurement is believed to be the main concern in diabetes patients, which is conveniently enabled by microwave sensors due to their instant response. A closed-loop insulin delivery system is an important step toward controlling hyperglycemia and hypoglycemia in individuals who need insulin injections to control their glucose level (Cobelli et al., 2011; Bruttomesso, 2019). Despite initial attempts (Blauw et al., 2016), some issues still remain unresolved with respect to continuous glucose monitoring. A reason to the instantaneous difference between typically measured and actual glucose level include sensor delay between the glucose level measured in the interstitial fluid compared to the blood level (10 minutes) and sensor malfunctions (Rodbard, 2016; van Doorn et al., 2021). A potential solution is to incorporate continuous glucose prediction to avoid natural latency and to interpolate missing measurements. Various configurations of machine learning algorithms have found interesting applications in microwave sensing in recent years (Xiao et al., 2020; Jeong et al., 2020; Aliramezani et al., 2020; Rahmani et al., 2020; Martínez-Nieto et al., 2019; Muckley et al., 2016; Kazemi et al., 2021a). In this article, we use the long-short-term memory (LSTM) network trained on the sensor data to predict future events 30 and 60 minutes in advance (van Doorn et al., 2021; Singh, 2017; Gecili et al., 2021; Rabby et al., 2021; Martinsson et al., 2020). Accurate predictions are also used to detect anomalies caused by missing a measurement or by a temporary unintended change in the measurement configuration. These techniques are studied in detail through this work in both *in-vitro* proof-of-concept experiments and human trials.

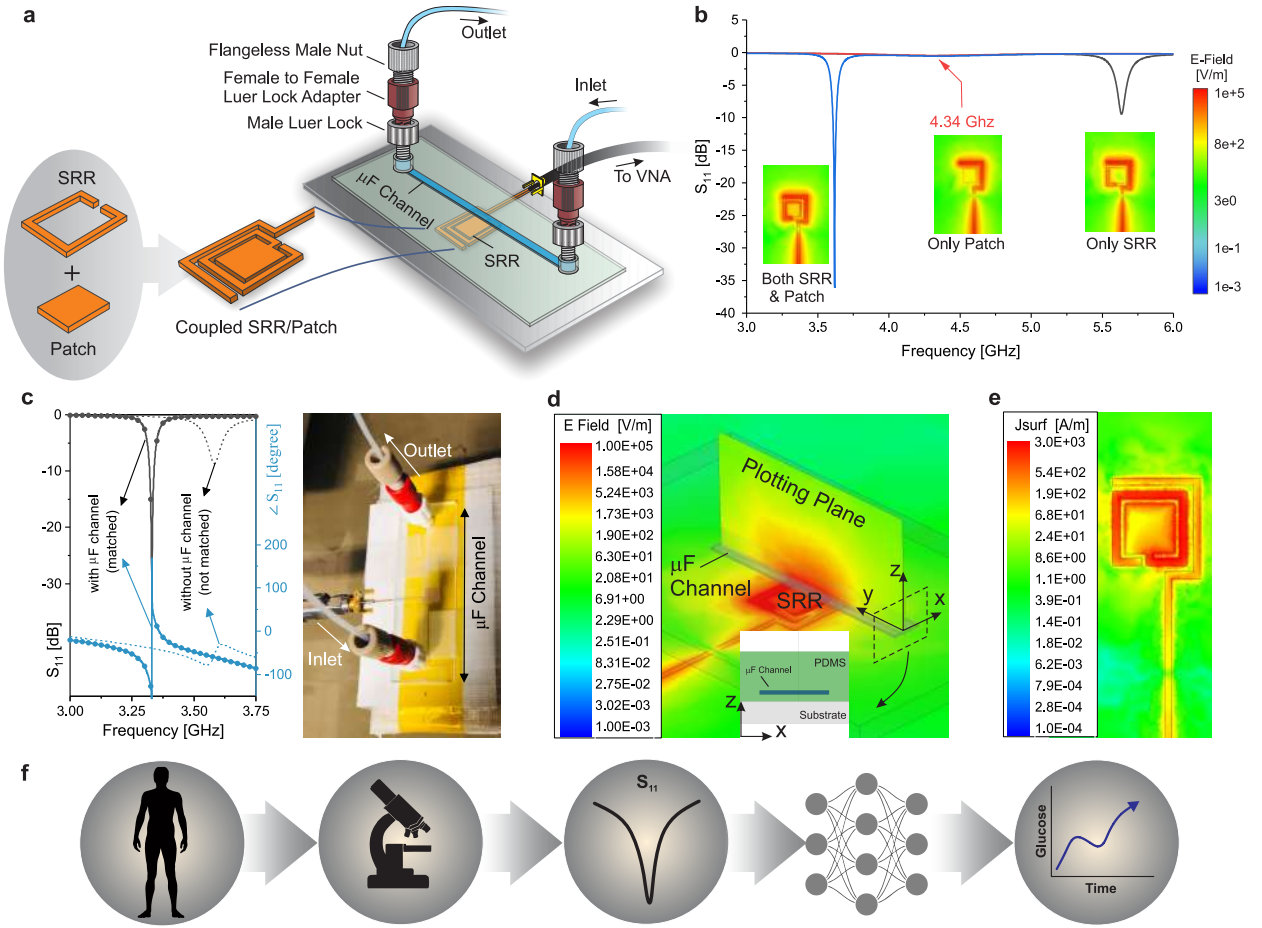


Figure 1: a Schematic of the proposed sensor with μF channel mounted. b The evolution of the sensor design with respect to its constituents (SRR/Patch). c Magnitude and phase simulation of S_{11} for both the sensor without μF channel (not matched) and with μF channel (matched) on top of it using Ansys Electronics (HFSS) (left) as well as fabricated sensor with μF channel on the right. d $|E|$ -field distribution is plotted at the frequency of resonance over the surface of the sensor with its cross section shown in the inset. The color bar shows the intensity of electric field. e Surface current density of the sensor with the μF channel at the frequency of resonance. f Generic paradigm of glucose level prediction by deep learning with respect to data processing through sensor interaction with human body.

2. Methods

2.1. Sensor simulation and fabrication

The sensor is designed at low ultrahigh frequencies (UHF), 3 GHz, enabling deep penetration of electromagnetic (EM) waves into tissues. The in-depth interaction of wave and matter in this frequency range helps to achieve high sensitivity for small amounts of analytes (more details are provided in the supplementary document). The initial conceptual design is based on a flexible substrate, which in this case is designed on a Rogers RO3003 substrate with the dielectric constant of $\epsilon_r = 3.3$, and loss tangent of $\tan(\delta) = 0.0013$, with 0.8 mm thickness. The sensor is printed on one side of the substrate, while the other side is fully covered with copper as an EM shield. This design increases the stability of the sensor response and reduces its susceptibility to environmental variations, such as the effects of proximity to surrounding objects.

The design criteria for the proposed sensor are the frequency of operation and the sensor size, which ensures its compatibility with flexible substrates. The loss factor from the glucose content affects the optimal frequency of operation as discussed in Supplementary Fig. 1. Geometrical form factor, on the other hand, is considered to be as compact as possible so that it can offer sensitive operation in a compact form and can be deployed at different locations on the body. The main concept behind the proposed sensor is the coupling between the underlying SRR and the loading

patch that the SRR fully surrounds (as shown in Fig. 1a) that eventually results in a miniaturized structure. This is a one-of-a-kind form of coupled resonators wherein SRR and patch are not completely identical resonators. In this combination, SRR is responsible for a highly sensitive region nearby the SRR gap while the patch considers deeper levels of body tissue due to its high gain characteristics. This very feature imposes the interaction of different resonance modes that results in a higher sensitivity due to glucose content at both high and low depths from the skin. Also, as evident from Fig. 1b, individual constituent parts (SRR and patch) are resonating at high frequencies of 5.65 and 4.34 GHz, respectively. However, with respect to the coupling between individual resonators, this design gives rise to a highly sensitive resonance at a significantly reduced frequency of 3.6 GHz (only sensor), which denotes a size reduction of 36% and 17% with respect to SRR and patch, respectively.

An open-ended transmission line is used to excite the resonator, surrounding it for better energy transfer. This single-port sensor measures the reflection from a resonator loaded by an external MUT. Compared to other transmission-based sensor designs, including the peak of resonance, the proposed sensor can be highly matched with respect to the MUT to achieve a low reflection. Furthermore, the transmission-based counterpart sensors suffer from degradation in the sharpness of the transmission response because the input power is either absorbed into the MUT-loaded resonator or propagates into the free space, which leaves low power received by the output. It has been found that when the loading material becomes lossy, the distance between the resonator and the exciting transmission line can be modified to change the external loading of the transmission line and achieve a high input impedance matching, and thus a deeper resonance profile. Another variation of the proposed structure can be a loss-compensated resonator discussed in (Kazemi et al., 2021b; Abdolrazzagli et al., 2023); however, since in that case the depth of resonance becomes extremely low, the sensor response stability degrades substantially and becomes highly vulnerable to environmental noise. Therefore, the focus of optimized sensor design is to utilize a reflection-based passive sensor, wherein the MUT is used as a part of sensor response matching in receiving maximum input power. More specifically, the sensor is designed to handle MUT loading. A well-matched sensor depends on its input impedance that varies with respect to its loading. Normally, when the sensor is designed with a desirable matching with a bare μF channel, the performance drops significantly when the MUT is introduced.

A μF channel with dielectric properties of $\epsilon_r = 2.9$ and $\tan(\delta) = 0.013$ at low UHF frequencies is used as the MUT carrier for *in vitro* tests (see Fig. 1a). The deployed μF channel is a hydrophilized polymethyl methacrylate (PMMA), purchased from Microfluidic ChipShop as a straight channel. The fluidic channel is connected to a flat lid with adhesive tape. The thickness of the lid is 175 μm , and the channel inlet and outlet are 58.5 mm apart. The thickness and width of the channel are 150 μm and 2.5 mm. The channel is secured on top of the sensor with proper taping. The inlet and outlet of the channel, aided with polytetrafluoroethylene (PTFE) fittings, including a male Luer lock, a female-to-female Luer lock adapter, and a flangeless male nut, are connected to two programmable syringe pumps. The effect of μF channel on the bare sensor matching can be avoided by modifying the physical resonator parameters toward better input impedance matching specified. The same strategy is applied for clinical trials with a separate sensor designed to consider the dielectric properties of human skin. This essentially adds a degree of freedom to the final product that can be customized according to the personal characteristics of a specific subject.

High-frequency simulations are performed using the Ansys Electronics Desktop simulator (HFSS). Figure 1c represents the magnitude and phase response of the sensor when optimized for low reflection with the channel above it. Deep resonances down to -34 dB are achievable for an empty channel at 3.326 GHz (matched), while the very resonator parameters yield a higher reflection when the channel is removed from the sensor (unmatched), shown with the dashed line. A fabricated prototype with the μF channel mounted on its top is shown in Fig. 1c. The sensor is fabricated using a high-precision milling machine from LPKF Laser and Electronics. The electric (E) field distribution at the resonant frequency is shown on the sensor surface in Fig. 1d. All gaps in the sensor are colored red, showing a high concentration of the E-field. This denotes a high coupling between the inner patch and the exterior SRR. For the purpose of this experiment, due to the limited width of the μF channel, only one gap is engaged. Sensor excitation is carried out through the open-ended transmission line that surrounds the sensor. This configuration allows for higher engagement of different resonator locations in receiving power from the input transmission line, leading to a better (deeper) matching of the sensor. The propagation of EM waves from the resonator to the surrounding medium is captured using E-fields in the plane that crosses the middle of the μF channel along the y-axis as shown in the inset of Fig. 1d. This shows how the sensor interacts with the surrounding materials non-invasively. Figure 1e represents the surface current distribution at the resonance frequency, where highly concentrated currents flow around the edges of the gaps, indicating a high potential for the currents to be disturbed by an external medium. Due to the special

configuration of the proposed sensor, one can use all sides of the SRR as a sensitive region with capacitive coupling, mainly due to the coupling between the SRR and the internal patch.

2.2. Data processing

In the proposed sensing system, depicted in Fig. 1f, the change in the total measured reflection profile (S_{11}) is expected to vary linearly since the variations in the GL are small (whether in water/ISF or in the body). Thus, using extra features in the analysis would only load the post-processing unit and make the proposed method computationally costly and unsuitable for real-time application. Therefore, only a single parameter is used as a representation of the GL changes. Since the variation in the frequency of operation is negligible, specifically for finer variations, it is replaced by the amplitude of the S_{11} depth, which varies linearly with GL in both *ex vivo* and *in vivo* experiments. Each measurement includes 3,001 frequency points (amplitude and phase of S_{11}), and the depth of the profile is processed as the single feature of the measurement. Measurements are performed using the S5065 vector network analyzer (VNA) with an IF bandwidth of 1 kHz; an average of 3 measurements is used for data processing. The initial postprocessing of the data is performed using a local LabView to find the minimum of S_{11} . The extracted feature is compared with the commercial sensor response and fitted with a line according to its linear behavior.

The sensor is used in successive patterns of increasing ISF GL concentrations (from 0 to 250, 275, and 500 mg/dL) for repeatability measurements. This pattern is called a 'cycle' with 90 data points at 5-s measurement intervals. The entire data set for this test is made up of repeating this cycle 164 times, resulting in a total of 14,760 data points. The prediction model, here LSTM, is trained only on normal data to learn normal patterns, and it is optimized for prediction accuracy. The dataset is divided into four subsets: 114 cycles for the training set (only normal values), eight cycles for the VN set (validation set without anomalies), 18 cycles for the VA (validation set that includes anomalies, 7 abnormal cycles augmented with 11 normal cycles), and 24 cycles for the test set (6 abnormal cycles augmented with 18 normal cycles). Several cycles are programmed differently to create anomalies in cycles: [65, 71, 73, 76, 79, 82, 147] in the VA set (with anomalies), [151, 153, 155, 158, 161, 164] in the test set.

For human trials, sensor data are recorded every 5 seconds for four subjects, one non-diabetic (female – F – age 35), one non-diabetic (male – M – age 30) and two diabetic patients (M – ages 34 and 28). Volunteers are asked to stay indoors and sit still in a chair with restricted and limited movement of their hands. Their fingers are securely attached to the sensor with proper taping to ensure that volunteers have a comfortable time during measurement. Each subject undergoes several intakes of food/chocolate during measurement at random times. These recordings are recorded for eight days, three hours a day. Since removing the finger and placing it back over days affects the sensor response's starting point, they are calibrated each day according to the commercial sensor so that all S_{11} recordings correspond to a certain commercially measured GL match across all days. Thus, the recorded data total 16,000 data points for a single person. Because the very dataset is used for GL prediction and anomaly detection, it is divided into known sections for training/validation/testing, since training needs to be conducted on normal time series. In this case, for each person, 10,000 data points are chosen for the training set, 1,000 for VN, 2,000 for VA, and 3,000 for the testing subset.

For both experiments, the training and VN data sets are transformed to a Gaussian distribution with zero mean and unit variance to standardize the data. A common oversight in this step could be to normalize the entire dataset, whereas the test set must remain intact during modeling. The statistics of the training set (mean and standard deviation) are then used to normalize the VA and testing sets. While transforming the data sets into the format required by the algorithm, each input sample is a roll of look-back number of timesteps to predict the desired future steps. This becomes a tensor (here a 3D array) with the dimension of (samples, look-back, number of features = 1).

2.3. LSTM prediction methods

In this work, an encoder/decoder LSTM is used for the prediction model that takes the most recent p values, also known as lookback, and outputs q future values, also known as lookahead. The network consists of hidden recurrent layers followed by an output layer. The number of hidden recurrent layers and the number of neurons in each layer are tuned using gradient descent optimization. Dropout is used to avoid overfitting between two consecutive layers, and the output layer is a fully connected dense layer with the number of neurons equal to lookahead, i.e. one neuron for each predicted future value. The activation function in the output layer is chosen to be linear for regression purposes, and the MSE is set as the loss function. With a look-ahead of q at time t , the model predicts the next q samples at $t + 1, t + 2, \dots, t + q$. The algorithm contains the following steps: The training set is used to train the prediction model. The best values for the model parameters, such as lookback, dropout, and learning rate, are extracted from Bayesian optimization. To avoid overfitting, VN is used for early stopping. Next, anomaly detection is enabled by exploiting

the prediction errors, the difference between the prediction made at time $t - 1$ and the input at time t , as anomaly indicators. These errors are then modelled using a Gaussian function with mean and variance computed from MLE. Then, anomaly scores are defined as the log probability density (PD) of the error vector, such that lower values indicate a higher likelihood of the observation being an anomaly. To set a threshold for the log PD values, the validation set VA is used that includes both normal and abnormal data, to reduce the likelihood of false positives. The two main assumptions used here are as follows:

- The prediction model is trained on the normal data set with no anomalies involved.
- The prediction errors follow the Gaussian distribution.

The lookahead of 150 is used to predict the next 30 minutes. In case of no interest in the future time steps, one can gain high accuracy with a lookahead of 1. It should be noted that the model parameters are optimized to minimize the prediction MSE and are expected to exhibit higher errors when dealing with anomalies present in the VA and test sets. However, there is a trade-off between the accuracy of long term prediction and that of anomaly detection. Therefore, the predictions-optimized parameters can be used as starting points for anomaly detection, with further manual tuning. A low MSE is required for the training set and a high MSE for the VA and the testing set since the latter contain anomalies. The cycles can be inspected from two perspectives. One with a longer time scale, and the other comprising three consecutive bumps with smaller time steps. If the LSTM states are wiped out at each batch or do not include information about the whole pattern period, then high prediction accuracy pushes the model to treat the anomalous data as normal ones; hence, this results in poor anomaly detection. Training the model is unsupervised with respect to the anomalies and there is no feedback to avoid fitting them. One solution to reduce false positives is to manually tune model parameters, e.g. lookback, number of recurrent layers, and number of neurons in each layer. Since the period of peaks is known to be 90 timesteps, with a slight change in the length of each period, the window size (lookback) is set to 90 to hold the states. Another method of keeping the states throughout an epoch is to use a stateful LSTM (Singh, 2017) mode with equivalent performance.

2.4. Selectivity analysis

To evaluate the selectivity of the sensor with respect to materials other than glucose (Product #G7021, Sigma-Aldrich, USA), several interfering items are added to the solution individually. The additional ingredients used in this analysis are fructose (100 mg/dL)(Product #PHR1002, Sigma-Aldrich, USA), caffeine (20 mg/dL)(Product #C0750, Sigma-Aldrich, USA), acetaminophen (15 mcg/mL = 1.51 mg/dL)(Product #A7085, Sigma-Aldrich, USA), galactose (5 mg/dL)(Product #G5388, Sigma-Aldrich, USA). ISF solutions with these contents are prepared and then glucose is added to the solution at a concentration of up to 100 mg/dL.

3. Results and Discussion

Initial sensor measurement includes bulk-medium sensing to evaluate the sensitivity at a fairly wide range of permittivity values. Figure 2a depicts the reflection parameter for the empty channel (air) as well as isopropyl alcohol (IPA), ethanol, methanol, acetone, and water in magnitude (left) and phase (right). Water is the main ingredient of interstitial fluid (ISF) that is a medium to mimic the subcutaneous fluid in the human body, which is used in our verification measurements. The sensor matching is engineered for the μ F channel so that a highly lossy medium such as water can also exhibit deep resonances down to -23 dB. The dielectric constant of water at low UHF frequencies is 76, which drops down to 61 due to the added glucose content (see Fig. 2b). In fact, a portion of high permittivity deionized water is replaced with glucose; the chemical reaction of these two substances also leads to a reduction in the permittivity. Moreover, water molecules interact with the hydroxyl groups on glucose to allow formation of an aqueous solution, which increases the effective loss factor of the solution. These changes are captured in each concentration's equivalent Debye model (more information is discussed in the supplementary file). Various glucose concentrations in ISF (detailed ingredients are given in the method section), including 100 mg/dL up to 400 mg/dL, are tested as shown in Fig. 2c. The resonant frequency shifts up slightly due to the permittivity reduction as the MUT loading reduces, while the amplitude of resonance change depends on the loading level from the MUT compared with the optimum load (matched case). In case of lower loading impact from MUT, frequency and amplitude variation trends are similar, whereas for higher MUT loading this trend becomes reversed. In this experiment, the amplitude increases as the solution becomes more lossy at higher concentrations (with loading impact less than matched load). Phase

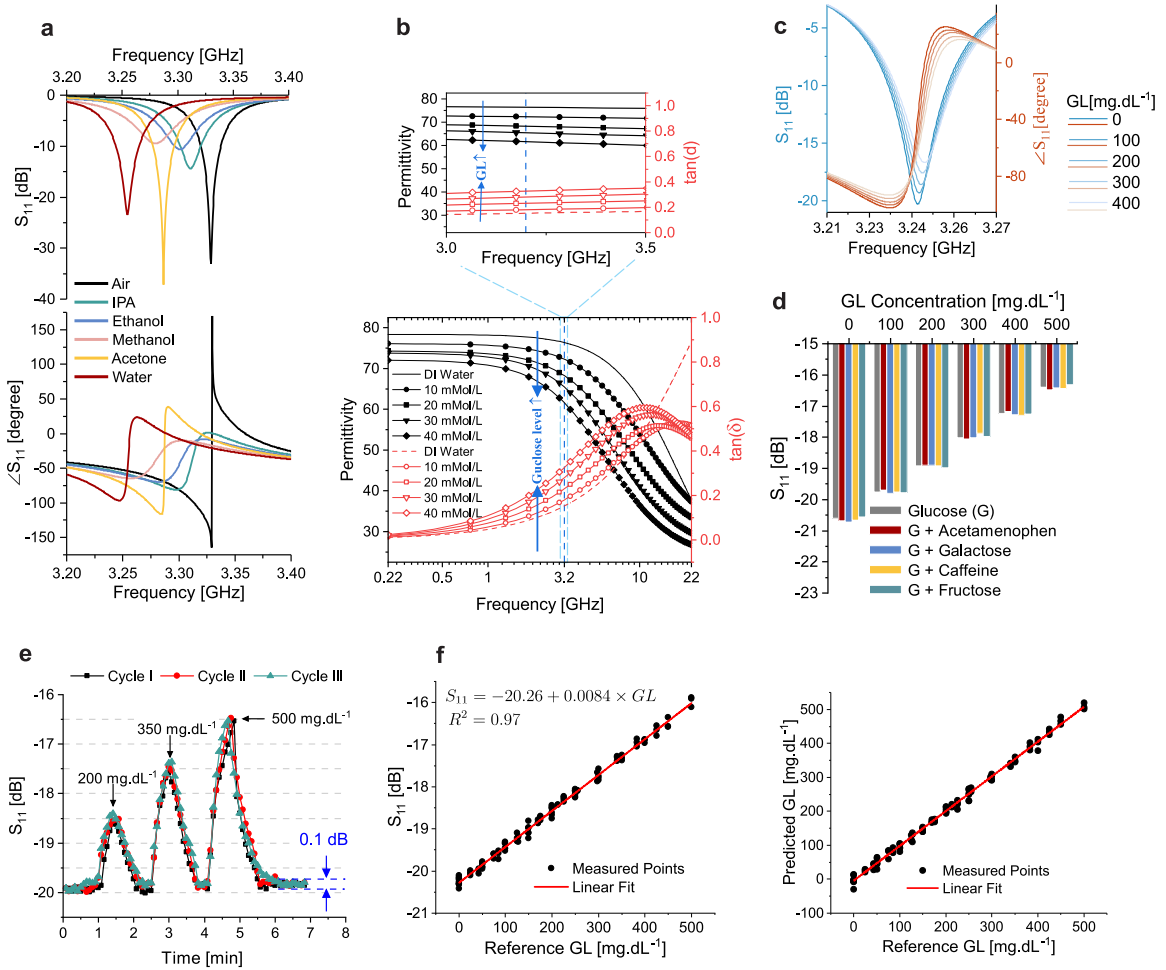


Figure 2: a S_{11} simulation result when the μ F channel on the sensor is filled with common chemicals (IPA, ethanol, methanol, acetone, water) with magnitude (top) and phase (bottom). b Dielectric properties of glucose in water solution for various concentrations of 0, 10, 20, 30, 40 mMol/L obtained from the Debye model. The inset represents detailed information in the frequency span of interest (3-3.5 GHz). c Measured results for various concentrations of glucose in ISF solution with magnitude (left) and phase (right) of S_{11} . Individual samples are prepared and shaken well for homogeneity and injected separately. The experiment is conducted when the materials and sensor are in equilibrium with the room temperature. d Selectivity analysis of the sensor with respect to interfering ingredients. ISF solutions with different glucose content (0, 100, 200, 300, 400, 500 mg/dL) are mixed with interfering analytes including Acetaminophen, Galactose, Caffeine, and Fructose. f Sensor reliability test. Two syringe pumps, one with highly concentrated glucose-ISF solution and another with only ISF solution, are employed to create different concentrations continuously. A pattern is configured to transit smoothly between the states of 0 \rightarrow 200 \rightarrow 0 \rightarrow 350 \rightarrow 0 \rightarrow 500 \rightarrow 0 mg/dL. This cycle is repeated two more times and the depth of S_{11} is measured at the frequency of resonance. b The sensor response is shown on the left, which is linearly fit with the reference GL. Estimation of GL with respect to measured S_{11} depth is shown on the right according to the linear fit for three cycles (right).

information also shows a reduction in the slope of the measured S_{11} values, indicating a higher loss content in the solution.

The selectivity of the proposed sensor is examined with respect to other similar ingredients, such as fructose and galactose. Also, with respect to the common lifestyle, acetaminophen and caffeine are also considered to be a possible part of human consumption. As a result, the relevant concentrations of each ingredient are individually combined with glucose levels of 0 to 500 mg/dL (covering the range from hypoglycemia to hyperglycemia) with increments of 100 mg/dL. Figure 2d shows the results of μ F channel experiment for this selectivity analysis. A slight variation is observed with respect to the level of extra interfering substances, while the main contribution is from the glucose itself. As a result, the proposed sensing technique is expected to respond selectively to glucose variations rather than to other interferents in the complex matrix inside the body.

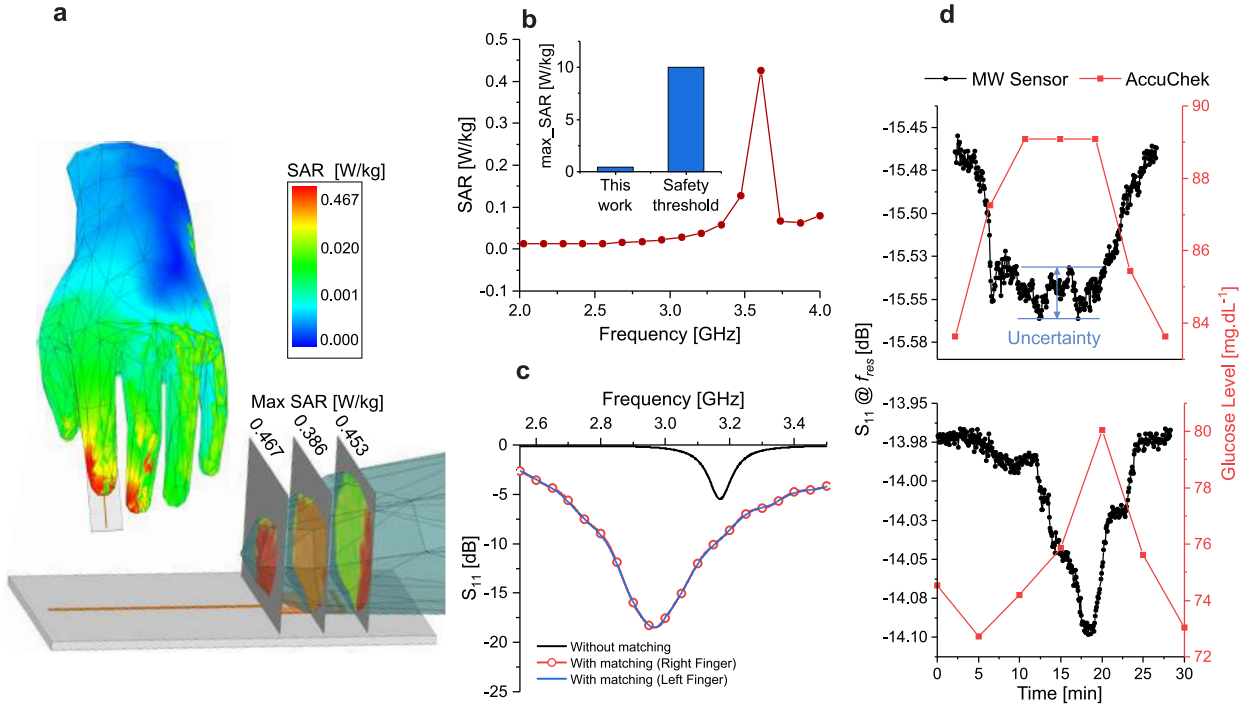


Figure 3: a SAR simulation results using HFSS on a human hand model that is positioned on the sensor. The inset represents the cross-sectional SAR plot on the index finger. b Maximum SAR values of the hand model are computed over a wide frequency range. The safety threshold of 10 W/kg is shown in the inset for comparison. c Initial verification of the sensor with finger. Black curve shows measured S_{11} when the finger is placed on the sensor that was originally designed for μ F channel. This experiment is repeated with a redesigned sensor while matching it with human skin dielectric properties. Measurement results for both right- and left-hand index fingers are shown in red/blue curves, respectively. d Calibration of the sensor with human finger for two different cases with respect to commercial glucometer AccuChek. A non-diabetic volunteer is asked to expose their right-hand finger to the sensor for 30 minutes while ingested chocolate (top). The sensor response is recorded every 5 seconds using LabView. A commercial glucometer is also used to sample the blood every 5 minutes for GL evaluation. The level of uncertainty in the sensor response for minimally changing GL is shown to be less than ± 1 mg/dL. This experiment is repeated in another instance (bottom) with a different chocolate intake profile.

3.1. ISF tests with repeatability analysis

The ISF solution is used for the next experiments (Supplementary Fig. 5a). The pH of the sample is modified to 7.2, close to the normal human level. Two pumps are engaged to produce the desired glucose concentrations in the ISF solution to feed the μ F channel (Supplementary Fig. 5f). To evaluate the sensitivity of the proposed sensor to glucose content, the whole range of human body GL is covered. Fasting GL values are typically lower than 100 mg/dL for non-diabetic persons and greater than 126 mg/dL for diabetic patients. Concentrations of 0 to 500 mg/dL in 3 successive peaks (peak 1: 0-200-0, peak 2: 0-350-0, peak 3: 0-500-0) are created, and this pattern is repeated three times to ensure the stability and repeatability of the proposed test setup. It is clear from Fig. 2e that there is a high coherence between similar peaks. The combination ratio between two pump injections creates the expected reference glucose content and is verified with a commercial glucometer. The recorded S_{11} values are compared with the reference values as shown in Fig. 2f (left). Since the variation in glucose content is small, the sensor operates linearly throughout the entire range of 0-500 mg/dL, with $R^2 > 0.97$ according to the following expression:

$$S_{11} [dB] = -20.26 + 0.0084GL [mg.dL^{-1}] \quad (1)$$

Therefore, mapping between the sensor response (in this case only the amplitude of resonance) and GL is possible using a linear expression. As a result, less computation is required. Data gathering for such a linear sensor response is faster, and thus better suited for commercial purposes. This hypothetical linear model between the sensor response and the expected GL is used to map all measured $|S_{11}|$ values to GL, resulting in predicted values as shown in Fig. 2b (right). In a more complex environment, other sensor parameters such as resonance frequency, quality factor, and resonance bandwidth can be used. This would be relevant, especially when external parameters such as temperature,

pressure, etc., adversely affected the sensor response. A concerning factor for microwave sensors is the safety limit of their wave propagation in the proximity of human tissues. This is typically measured with the specific absorption ratio (SAR), which indicates the level of absorbed power averaged over 10 grams of tissue. Full-wave simulations reveal that SAR values are high near the fingertip compared to other parts of the hand when the index finger is placed on top of the sensor (see Fig. 3a). As shown in Fig. 3b, a fair margin is obtained for SAR values (with a maximum of 0.467 W/kg) compared to the safety threshold of 10 W/kg over a wide range of frequencies (2-4 GHz). This reassures the safety of the proposed sensor when used as a wearable device.

3.2. Sensor calibration for sequence-to-sequence modeling

In the next step, the sensor is exposed to the human body to evaluate its effectiveness in interrogating the blood GL and to confirm its real-time functionality. In this regard, four different persons including two non-diabetics, one type 1 diabetic, and one type 2 diabetic have been chosen for noninvasive monitoring. The sensor is confined within a small size such that it can be used on various locations of the body including, but not limited to, finger, arm, ear lobe, abdomen, etc. In this work, the sensor size is chosen small enough to be fully covered with a single index finger. It should be noted that the sensor has been redesigned with a slightly modified size optimized for human body loading conditions (Supplementary Fig. 4), different from the μF channel loading. This is verified in an initial measurement, as shown in Fig. 3c. When the sensor for μF channel is used for finger measurement, the response dies out due to the excessive loss of the skin. However, the redesigned sensor exhibits a deeper resonance with a finger placed on it in comparison with a bare sensor. Similar results are obtained when the index fingers of the right and left hand of a person are exposed to the sensor. This confirms that the sensor provides consistent results as long as the positioning of the finger on the sensor surface is controlled and secured. For this purpose, the finger is placed inside a hollow partition inside a holder made of acrylic known as Poly Methyl Methacrylate (Supplementary Fig. 5 d-e). Minor discrepancies are expected due to the nature of planar design, but this can be avoided with firm wearability and secured configuration. Measured S_{11} values are shown when the right index finger is being monitored for 30 minutes and the sensor response is recorded every 5 seconds using LabView for calibration purposes. The sensor measures the effective change of the skin dielectric constant according to variations in the blood glucose content. The reflection depth of the sensor is compared to the commercial glucometer, Accu-Chek, every 5 minutes. Each person starts in fasting condition and is fed a specific amount of chocolate bar at known times. It is clear from Fig. 3d that the trends are inversely proportional, mainly because of the way the sensor is loaded with a human skin. Indeed, there is an optimum loading for each resonator that results in the lowest possible reflection (minimum of S_{11}) at matched condition resonance frequency f_0 . While with a different loading from the environment, here the skin, the resonance frequency f_{res} might be slightly off to the left or the right side of f_0 . In the case of $f_{res} < f_0$, the upshifts in the f_0 due to the reduction of effective permittivity at higher glucose concentrations lead to a lower $|S_{11}|$, which is expressed with inverse proportionality between S_{11} and the GL. In contrast, for the case of $f_{res} > f_0$, $|S_{11}|$ starts to increase in parallel with GL. This is not abnormal in a sensor designed to operate close to its optimum input matching point. To increase the trustworthiness of the sensor, it is also calibrated for all four persons involved (only two are shown for brevity). The GL measurements obtained using the commercially available glucometer are interpolated using cubic B-splines to generate intermediate results to match the number of S_{11} measurements. Once these two sets are compared, it is confirmed that the inverse proportionality follows a linear trend between the $|S_{11}|$ and GL with a high Pearson correlation $r = -0.93$ for Fig. 3d (top) and $r = -0.95$ for Fig. 3d (bottom).

In diabetic patients who have GL higher than 126 mg/dL while fasting (no food consumption for at least 8 hours), it is crucial to keep control of GL to avoid possible complications. These include vomiting, rapid heartbeat, vision concerns, and other symptoms. Patients at increased risk of hyperglycemia should keep their GL low, either through physical activities or by a limited food intake plan. In addition, continuous monitoring of GL in the blood can help prevent most hyperglycemia-related problems well in advance. In this work, we introduce a monitoring system composed of a machine learning algorithm coupled with a flexible microwave sensor. The fingertip is flushed on the planar sensor, which enables deeper interrogation of the skin layers through the wave propagation. The system tracks and predicts GL values and signals when they pass the undesired threshold or are likely to do so within the next 10-20 minutes as shown in Fig. 4. To demonstrate the predictive functionality of the proposed system, various concentrations of glucose are generated with the combination of two syringe pumps in a repetitive pattern representing low (max GL = 250 mg/dL), medium (max GL = 375 mg/dL), and high (max GL = 500 mg/dL) peaks of glucose content in the ISF solution as shown in Fig. 5a. The 3-peak cycles containing 90 points are repeated and measurements are recorded every 5 seconds with LabView. The corresponding $|S_{11}|$ values show normal behavior until certain periods

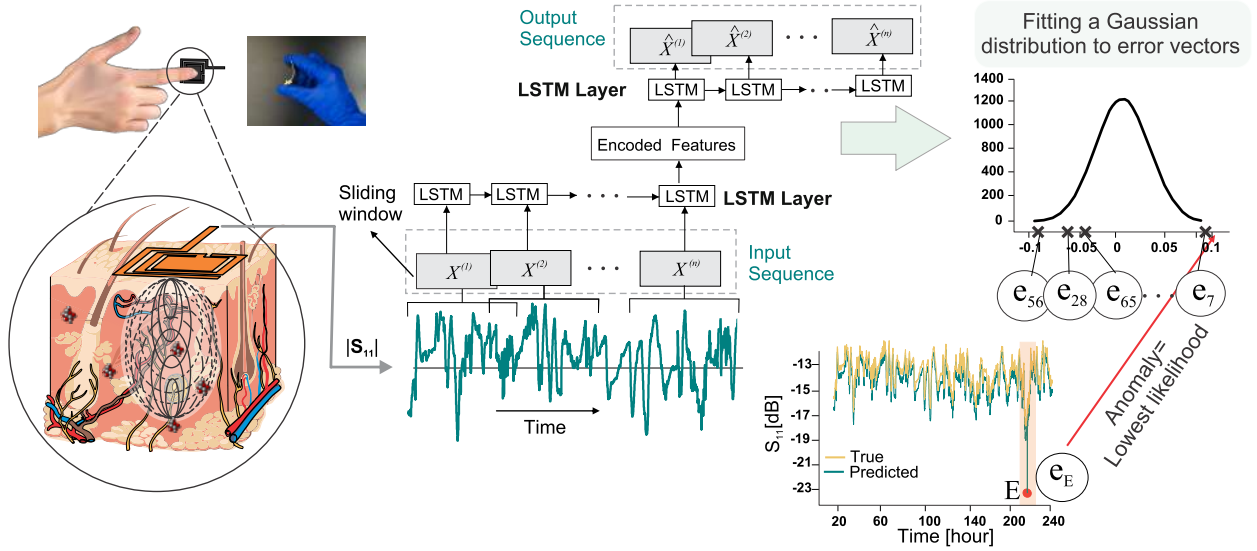


Figure 4: An overview of Multistep LSTM system, our predictive learning framework for glucose monitoring. The measured S_{11} amplitudes are combined and used as the input of a deep learning model that predicts GL. Next, the error vectors are modelled by a Gaussian distribution, where the lowest likelihood at the tail of this distribution represents an anomaly occurred during data recording. Anomalies include excessive pressure on top of the sensor, sudden change in the temperature, data inconsistency, and hand movement; LSTM: long short-term memory network.

when deliberate anomalies are introduced into the system. This is achieved by modifying the pattern program of the injecting pumps so that some of the regularly expected peaks are removed. In total, 14,757 data points are recorded as time series. This data set is constructed with two major goals for the sensor system development: to predict future values and to detect possible anomalies. Predicting future steps provides an early indication of the upcoming behavior, and this can be used as a sign of an anomaly. An anomaly can be an outlier data point, which in this case can be due to a short-time environmental disturbance such as a sudden change in the temperature, humidity, or proximity of an adjacent object. Another common type of anomaly that can be present in time series is a behavior that introduces an unusual phenomenon disrupting the periodic pattern. Long sort term memory (LSTM) is a neural network that can be used for time-series analysis. A multistep LSTM is built using the time-series data and deployed to reconstruct a new sample and predict the next step. In this model, a window of a limited number of samples, also known as lookback or timestep, is chosen as one segment of the input sequence to the LSTM network. This window slides over the entire dataset. The encoded features are then fed to the decoder to calculate the predicted output sequence, as shown in Fig. 4. The prediction error is calculated as the difference between the prediction made at $t-1$ and the input value at time t of the training data. A loss function, formulated as the mean squared error (MSE), is used to evaluate the success rate of the model. The accuracy of the prediction versus lookback number is examined with the MSE loss for the train set and is shown in Fig. 5b that is minimized at lookback of 90. The values of MSE loss for training, validation (including anomalies), and test (including anomalies) datasets are, respectively, 0.022, 0.0849, and 0.0514, after 500 epochs. In the case of detecting anomalies, the confusion matrix serves as a comprehensive evaluation tool encompassing four critical categories: 'True Positives' (TP), 'False Positives' (FP), 'False Negatives' (FN), and 'True Negatives' (TN). TP and TN signify correctly identified anomalies and normal data, respectively. In contrast, FP and FN represent inaccuracies where normal data is misinterpreted as an anomaly, and anomalies are overlooked as normal data, respectively. A detailed confusion matrix is shown in Fig. 5c. The error between predicted and measured $|S_{11}|$ values in train set is obtained for the well-trained system as shown with histogram of Fig. 5d. The relationship between the measured and predicted $|S_{11}|$ values of this sequence is described as a linear fitting with $R^2 = 0.974$ (Fig. 5e).

Microwave sensors with high sensitivity are prone to environmental interferences mainly due to their open structure and ease of interaction with the surrounding medium. This vulnerability limits the range of applications and reduces its effectiveness in dealing with a complex medium. Anomalies introduced by the environment are likely to exacerbate the sensor output precision, hence an anomaly removal unit is crucial to ensure the sensor performance robustness. The anomaly detector uses the increased values of prediction errors as anomaly indicators. The prediction errors obtained

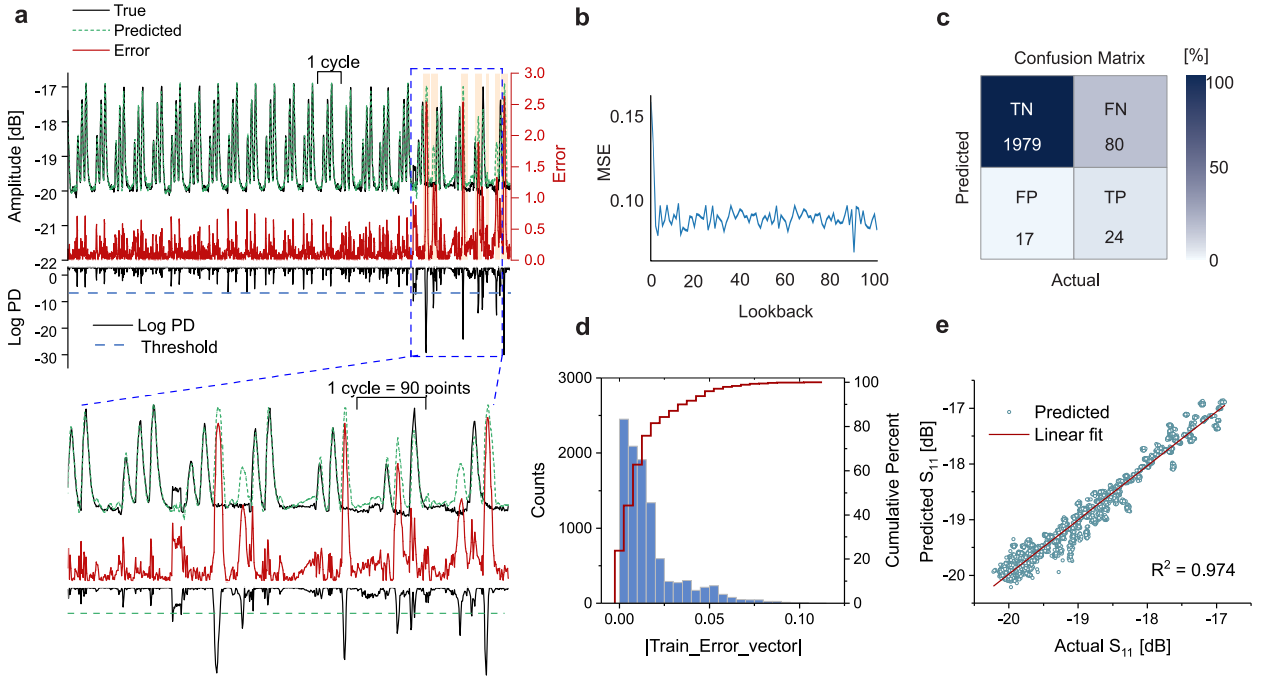


Figure 5: a The glucose content in the ISF is tested using a μ F channel and a programmed pattern of glucose injections. At certain points, the regular pattern is intentionally broken to introduce anomalies. The error between the measured sensor response and the expected (predicted) response is also depicted. Log PD elaborates on the likelihood of a data point to be an anomaly. A subsection of this pattern is shown in the bottom with more details on the anomalies. b Training error MSE on the repeatability dataset for different number of lookbacks. The optimum value for this parameter is achieved at 90 for a single timestep. Increasing lookback number will not improve the prediction performance of the network. c Confusion matrix for anomaly detection in μ F channel test. d Density distribution of absolute error vector for training set in the repeatability dataset is demonstrated as both histogram and cumulative percentage. e Predicted S_{11} correlation with the actual S_{11} values. The line shows a linear correlation (R^2) between experimentally measured S_{11} amplitudes and the predicted values using LSTM.

using training data are modelled using a Gaussian distribution, with parameters (mean and variance) computed by maximum likelihood estimation (MLE). The errors at the end of this distribution are concluded to be anomalies (see the supplementary file for more detailed information). On unseen data, the log probability densities (PDs) of errors are computed and used as anomaly scores. The detection of anomalies depends on the level of log PD values such that a lower log PD value (more negative) indicates a more unusual onset. A threshold of log PD is set using the validation dataset, which contains both normal data and anomalies. This threshold helps to separate anomalies from normal data and minimize the number of false positives. The predicted samples from the multistep LSTM are plotted in the top graph of Fig. 5a, along with the true test set values and several highlighted anomalies. In this case, peaks removed from the primary dataset using programmable syringe pumps are considered as anomalies. A more detailed analysis on the μ F channel using ISF is given in supplementary Fig. 6.

3.3. In vivo test for non-invasive monitoring of glucose.

In this study, four volunteers were recruited after having human ethic approval, without discriminatory intent based on sex, age, occupation, race, or ethnicity. All used their right-hand index finger with the sensor while their hand was secured on the table with proper tapping and a fixed holder for the finger. They were asked to keep physical movement at the lowest possible level. GL of each participant was recorded every 5 seconds, while their finger-pricked blood GL were taken at random intervals due to the limited number of test strips available. At random points of measurement, the sensor response was compared against Accu-Chek level; high agreement was confirmed throughout the experiment. Furthermore, the participants ingested 45 g of chocolate bar with 30 g of total carbohydrates (22 g sugar content), and their corresponding blood GL was continuously monitored.

The blood GLs of four different individuals with various conditions are continuously monitored. The following subjects are included in the trials: non-diabetic male, non-diabetic female, and two diabetic males (type 1 and type 2).

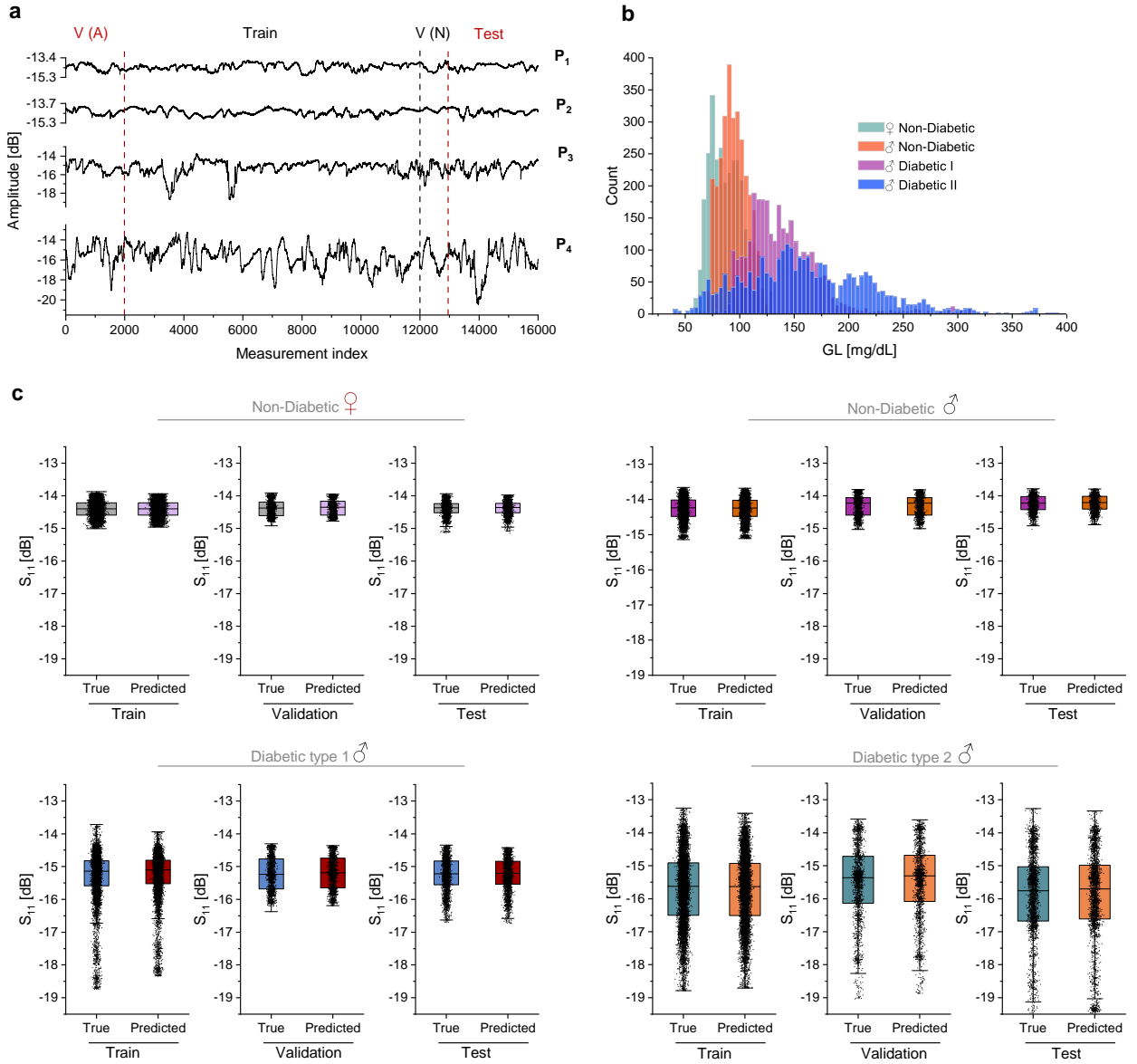


Figure 6: a The sensor is used to monitor index fingers of 4 different persons with 5-second recording intervals and measure the depth of S_{11} amplitude values. Participants ($P_1 - P_4$) include one non-diabetic (P_1 : female – age 35), one non-diabetic (P_2 : male – age 30) and two diabetic participants ($P_3,4$: male – ages 34 and 28). Each person receives chocolate at random times during the measurement. The whole time series data per person is obtained over eight days, three hours a day. b Measured S_{11} values are converted into corresponding GL values according to a linear fitting curve ($GL [mg/dL] = -50 (S_{11} [dB] + 12.5)$). Histograms of measured GL with the microwave sensor for all participants. c Distribution of actual and predicted S_{11} amplitude in three sets of train, validation (VN), and test for every person. In the box plots the central line defines the median. The lower and upper hinges of the boxes correspond to the 25th and 75th percentiles, and the whiskers are the minimum and maximum values.

The sensor response measured for each person includes 16000 datapoints that are recorded at 5-second intervals for eight days. Each day, 2000 datapoints are recorded per 3-hour sitting. During concatenation of daily measured data points, if there is a sharp contrast between the GL of the end and start points of adjacent days, it is considered as an anomaly. To verify that the measured data agree with the real GL, an AccuChek glucometer is used as a commercial gauge to measure the GL every 10 minutes. This frequency of measurements with AccuChek is high enough to capture all variations consider limited number of test strips. This verification is carried out for a few datapoints due to the

limited number of test strips. This fact check confirms a high correlation between the commercial sensor and the proposed sensor response (supplementary Fig. 12-15). The data set shown in Fig. 6a consists of a training set, a testing set, a validation set that includes anomalies VA, and a validation set without anomalies VN. The individual subsets are separated by vertical dashed lines. The measured $|S_{11}|$ values are converted into equivalent GLs according to the linear relationship obtained between measured $|S_{11}|$ and GL measured by the commercial AccuChek as follows:

$$GL [mg/dL] = -50 (S_{11} [dB] + 12.5) \quad (2)$$

A histogram consisting of GLs computed from eq. 2 for four participants is shown in Fig. 6b, which demonstrates a meaningful range for each person.

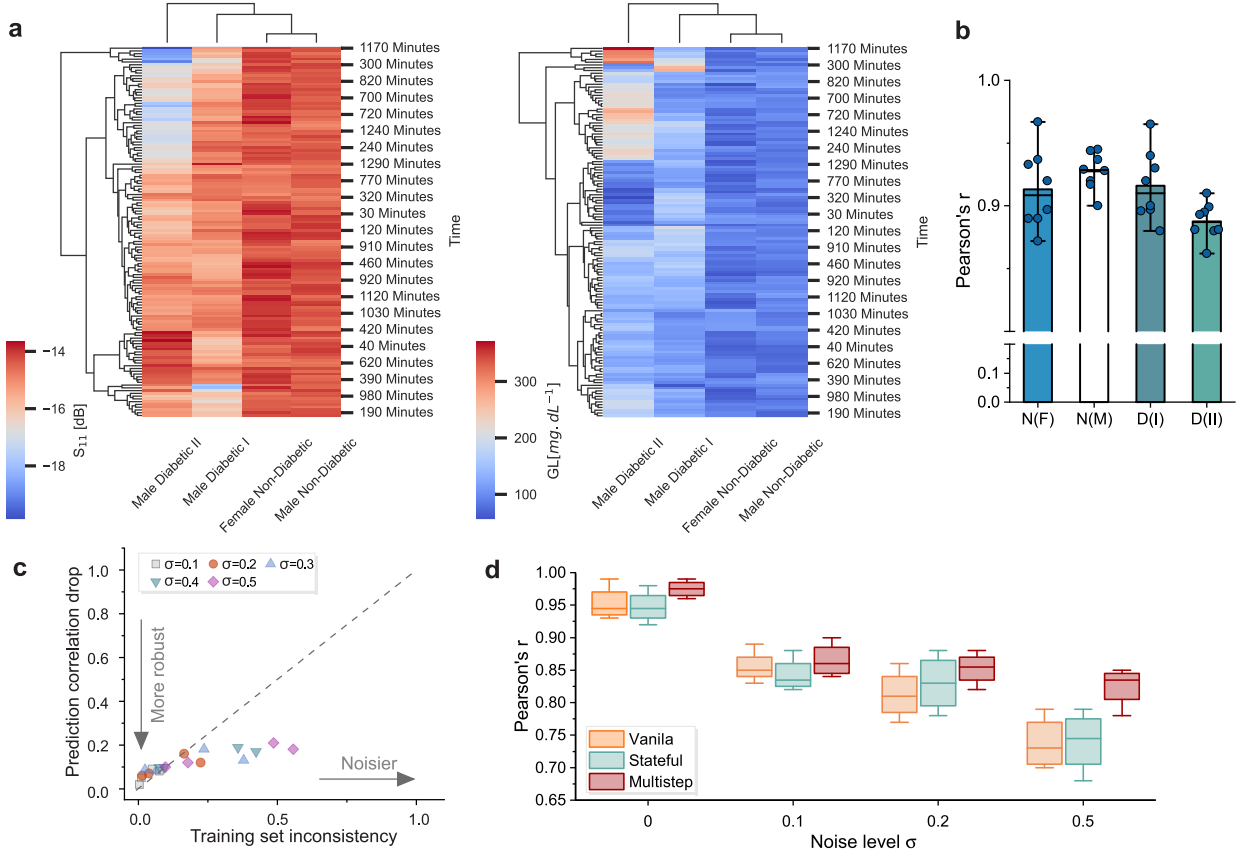


Figure 7: a Heatmap of all measurement time intervals are clustered by similarity. Both dendrograms are color-coded to represent S_{11} values on the left and corresponding measured GL using a commercial glucometer on the right. The color inversion between these illustrations is because of inverse proportionality between S_{11} value and GL. b Microwave sensor measurement results are split into three-hour intervals (Supplementary Fig. 1-4). Pearson correlation of each window between S_{11} (measured using MW sensor) and GL (measured using AccuChek) is obtained for all four participants (N(F): non-diabetic female, N(M): non-diabetic male, D(I): type 1 diabetic male, and D(II): type 2 diabetic male). c The training set related to each participant is perturbed by a random noise with normal distribution $N(0, \sigma)$ to evaluate the model robustness. Five noisy training sets are simulated using $\sigma = 0.1, 0.2, 0.3, 0.4,$ and 0.5 , and a separate LSTM model is trained on each training set. Then the trained models are evaluated on the intact test sets. Pearson correlation between pre- and post-perturbed values of the training dataset is considered as r and the training set inconsistency is $1-r$. A scatter plot shows the performance of the network for every participant at different noise levels. d Comparison between Vanilla, Stateful, and Multistep models on noise-free training set and noisy test datasets at different noise levels with $\sigma = 0.1, 0.2,$ and 0.5 . The midline of box plots represents the median. The lower and upper hinges of the boxes correspond to the 25th and 75th percentiles, and the whiskers are the minimum and maximum values.

The multistep LSTM is used to model this dataset, and the predicted values are obtained after 100 epochs for each person. The loss of the test set becomes as low as 0.0041, 0.0077, 0.015, 0.091 for subjects 1-4, respectively. The predicted values of the sensor response are compared with the actual values in Fig. 6c. LSTM-based predictions for the train, test, and validation sets are summarized with a box plot against their corresponding actual values. This

comparison for all 4 participants reveals a similar range of datapoints that supports high fidelity of the prediction system. To evaluate the correlation between various instances of a person's GL, the heat map of the measured $|S_{11}|$ and the GL measured by AccuChek is plotted in Fig. 7a. These heatmaps comprise each person's measured values sampled at 10-minute intervals. As a result, the similarity between the sensor response and the actual GLs is ensured according to the way in which the participants are clustered identically. Furthermore, the sensor-measured response ($|S_{11}|$) and the actual GLs determined by AccuChek are also shown in detail for each 3-hour sitting as given in the Supplementary Fig. 12-15 for all four participants. In these figures, a separate mapping is used for each 3-hour window for high accuracy. The Pearson correlation value is then calculated for 8 windows per person and is plotted in Fig. 7b. The whiskers of the box plot illustrate the minimum and maximum correlations. A high overall correlation is achieved that suggests a high-fidelity sensor performance while being used by different participants provided that a separate calibration fit is used per person.

The proposed sensor is a generic prototype that is designed to be used by a broad range of customers. As a result of various operation environments, the measurement conditions might not be always ideal, which requires the consideration of noise in the training set. The LSTM model used in this work is examined with various noisy training sets. Next, a separate prediction is conducted over the total measured sequence of a participant. Then, the correlation between the actual sensor response and the predicted response according to a noisy training set is computed. The added noise follows a normal distribution with zero mean and different standard deviations of $\sigma = 0.1, 0.2, 0.3, 0.4,$ and 0.5 . In each case, training set is correlated with the noise-free training set to calculate the Pearson correlation r , which is used to define the training set inconsistency as $1 - r$. It is shown in Fig. 7c that the prediction model is robust against the added noise as the correlation drop is not linear with the data inconsistency. This result is also compared with other well-known LSTM models, namely, Vanilla and Stateful. Figure 7d represents comparative Pearson correlation for all four participants using a box plot. It is found that the multistep LSTM outperforms the other methods, which suggests its potential as a highly stable and robust predictive system.

A brief analysis of this modeling is shown in Fig. 8a, which represents an exemplary test set for a non-diabetic male participant (more detailed for all participants' results can be found in the supplementary Fig. 12-15). The results show that an accurate prediction is obtained for each person in both upward and downward trends of the body GL. The real-time prediction of the output values from the sensor response indicates that there is no time lag between the measured GL of the body at the frequency of operation. For each subject, deliberate anomalies are introduced during each measurement. Anomalous periods are highlighted, and the plots confirm that the prediction errors also become large during the same intervals. The anomalies are created by several means, including sudden lifting off the finger and returning it to approximately the same position, strong tapping on the table holding the sensor, and temporarily changing the temperature in close proximity of the sensor. A suitable threshold is chosen for log PD values of individual subjects to avoid false positive anomaly detection, which is showcased in detail in the supplementary file, Fig. 16. The corresponding GL for each measured S_{11} depth is obtained according to the initial calibration of the sensor with respect to each subject, similar to the case shown in Fig. 8a. The train and validation loss for each person converge at 100 epochs; however, only 20 epochs are shown for brevity in Fig. 8b. The mean loss values from four persons are shown with symbols and the boundary is created with respect to the maximum and minimum loss values among all participants (see Supplementary Fig. 15 for train error analysis). The histogram of the measured sensor response ($|S_{11}|$) in the test set is compared with its predicted $|S_{11}|$ in Fig. 8c for an exemplary case of the non-diabetic male participant that showcases the predicted values follow the same distribution as the actual ones. Detailed histograms of the test/train/validation sets of all participants are given in the Supplementary Fig. 17. The left-skewed distribution of this test set deviates slightly from a normal distribution. The measured $|S_{11}|$ is modelled with a normal distribution with respect to the test set's mean and standard deviation. Figure 8d shows that the measured sensor response deviates from the normal distribution close to the tails, which also corroborates with the result of histogram. The Pearson correlation r is also used to elaborate the similarity between the measured sensor response and the predicted values from the LSTM model in Fig. 8e, where a high $r = 0.9937$ reveals a good agreement between predicted values and the real ones. To elaborate on the repeatability of the proposed technique, the Clarke error grid (CEG) analysis for all four subjects is shown in Fig. 8f. It is clear from the inset information of the graphs that the estimated GLs fall 100 % within clinically acceptable zones. This can be broken down as A: 99.89 %, B: 0.1 % for non-diabetic person (F), A: 98.3 %, B: 1.17 % for non-diabetic person (M), A: 99.43 %, B: 0.56 % for type 1 Diabetic (M), and A: 99.69 %, B: 0.3 % for type 2 Diabetic (M). The parameters of interest in evaluating the performance of the proposed sensor are the root mean square error (RMSE), the mean absolute relative difference (MARD), and the mean absolute error (MAE).

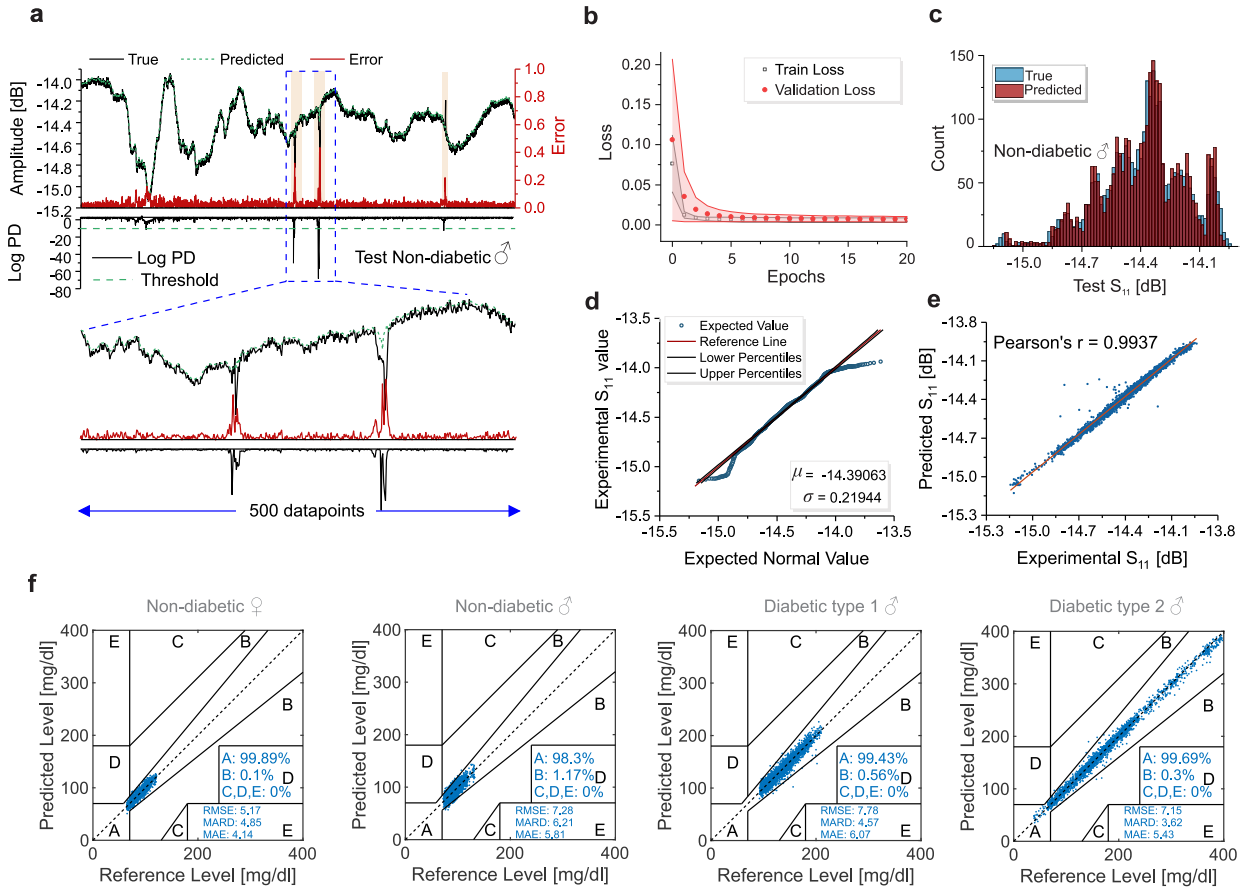


Figure 8: a Prediction and error vector of a male non-diabetic male participant is depicted with 3000 datapoints as an exemplary test set showing predicted S_{11} values from the LSTM model, error vector values, and Log PD. A more detailed view of the test set is extracted containing only 500 datapoint and is shown below. b The LSTM model convergence is depicted using training set- and validation set-loss. Out of total 100 epochs of this modelling, only 20 epochs are shown for presentation clarity. The convergence curves for each participant are used to create the band error plot containing mean values (symbols) and the error band (bounded by minimum and maximum values). c Comparison between the measured and predicted S_{11} values in the test set of the non-diabetic male participant is shown. This also showcases the measured values have a left-skewed distribution, which typically depends on the person's health factors. d A normal distribution is modelled based on the measured S_{11} values with $\mu = -14.39$ and $\sigma = 0.21944$. A Quantile-Quantile plot compares the measured dataset and the modelled normal distribution, which shows deviations closer to the tails indicating the data to be flatter than a normal distribution (platykurtic). e Pearson factor between the measured S_{11} values and the predicted value by the LSTM model reveals a high correlation of $r = 0.9937$. f Clarke error grid analysis results are evaluated based on measured S_{11} values converted into GL using a linear fit for each participant. The measured datapoints reside mainly within zone A and marginally in zone B. Error analysis metrics including RMSE, MARD, and MAE are also given in the inset.

These measures are provided with detailed information in the inset of Fig. 8f. These percentages, obtained for a total of 3,000 test data points, show a good match between the measured sensor response and the reference GL.

Implementation of this sensor is based on single frequency operation due to the high sensitivity of the depth of S_{11} . This reduces the complexity of using bulky VNAs into a simpler readout circuit similar to a low-frequency radar board (Omer et al., 2020) or frequency demodulation scheme (Hitzemann et al., 2022). In such a portable configuration, only single frequency generation is required with power as low as -10 dBm (100 μ W) for reflection measurement purposes. Regarding deployment of LSTM and the anomaly detection algorithm, predictions typically occur within milliseconds, once the system has been trained. This is sufficiently fast for predicting future events in the next 30-60 minutes.

4. Conclusion

The proposed sensory system comprises a microwave sensor, in which two smaller resonators are coupled to form an ultrasensitive region for material sensing. The sensor is noninvasive, compact, low profile, and ultimately wearable

for a continuous analyte monitoring scheme unlike enzyme-coupled electrochemical sensors. Sensor performance is enhanced by embedding a predictive neural network platform, using which the future trend of changes in the environment is followed in real-time. In addition, to ensure accurate predictions, the characteristics of the proposed planar sensor naturally susceptible to environmental impacts are mitigated using an anomaly detection algorithm. The resultant sensor has great potential of being deployed in highly sensitive applications for noninvasive interrogation of the ambient interstitial glucose levels.

Declaration of competing interest

The authors declare that they have no known competing financial interests or personal relationships that could have appeared to influence the work reported in this paper.

Data availability

Data supporting the findings of this study are available within the article and its supplementary information files.

Code availability

The source code of our deep learning model and data analysis scripts available on GitHub address. Note: The code will be public once the paper becomes accepted. A pdf version of the code is available for reviewers.

Acknowledgements

This work was supported by (P.E.L.) the Canadian Institutes for Health Research and the Alberta Diabetes Foundation, the Natural Science and Engineering Research Council (NSERC) of Canada, Future Energy System (FES), and CMC Microsystems. The authors would like to thank the Rogers Corporation for their substrate donation. The authors would also like to thank Janyne Johnson for material preparation.

CRedit authorship contribution statement

Nazli Kazemi: Conceptualization of this study, Methodology, Testing. **Mohammad Abdolrazzagli:** Conceptualization, Methodology, Software, Editing. **Peter E.Light:** Supervision, Editing. **Petr Musilek:** Supervision, Methodology, Editing.

References

- Abdolrazzagli, M., Daneshmand, M., 2020. Exploiting sensitivity enhancement in micro-wave planar sensors using intermodulation products with phase noise analysis. *IEEE Transactions on Circuits and Systems I: Regular Papers* 67, 4382–4395.
- Abdolrazzagli, M., Daneshmand, M., Iyer, A.K., 2018. Strongly enhanced sensitivity in planar microwave sensors based on metamaterial coupling. *IEEE Transactions on Microwave Theory and Techniques* 66, 1843–1855.
- Abdolrazzagli, M., Katchinsky, N., Elezzabi, A.Y., Light, P.E., Daneshmand, M., 2021. Noninvasive glucose sensing in aqueous solutions using an active split-ring resonator. *IEEE Sensors Journal* 21, 18742–18755.
- Abdolrazzagli, M., Kazemi, N., Nayyeri, V., Martin, F., 2023. Ai-assisted ultra-high-sensitivity/resolution active-coupled csrr-based sensor with embedded selectivity. *Sensors* 23, 6236. doi:10.3390/s23136236.
- Agustini, D., Bergamini, M.F., Marcolino-Junior, L.H., 2017. Tear glucose detection combining microfluidic thread based device, amperometric biosensor and microflow injection analysis. *Biosensors and Bioelectronics* 98, 161–167.
- Albishi, A.M., El Badawe, M.K., Nayyeri, V., Ramahi, O.M., 2020. Enhancing the sensitivity of dielectric sensors with multiple coupled complementary split-ring resonators. *IEEE Transactions on Microwave Theory and Techniques* 68, 4340–4347.
- Aliramezani, M., Norouzi, A., Koch, C.R., 2020. A grey-box machine learning based model of an electrochemical gas sensor. *Sensors and Actuators B: Chemical* 321, 128414.
- Amir, O., Weinstein, D., Zilberman, S., Less, M., Perl-Treves, D., Primack, H., Weinstein, A., Gabis, E., Fikhte, B., Karasik, A., 2007. Continuous noninvasive glucose monitoring technology based on “occlusion spectroscopy”.
- Azimi Dijvejin, Z., Jain, M.C., Kozak, R., Zarifi, M.H., Golovin, K., 2022. Smart low interfacial toughness coatings for on-demand de-icing without melting. *Nature communications* 13, 1–12.
- Badugu, R., Lakowicz, J.R., Geddes, C.D., 2005. A glucose-sensing contact lens: from bench top to patient. *Current opinion in biotechnology* 16, 100–107.

- Baghelani, M., Abbasi, Z., Daneshmand, M., Light, P.E., 2020. Non-invasive continuous-time glucose monitoring system using a chipless printable sensor based on split ring microwave resonators. *Scientific Reports* 10, 1–15.
- Bariya, M., Nyein, H.Y.Y., Javey, A., 2018. Wearable sweat sensors. *Nature Electronics* 1, 160–171.
- Barrett, P.M., Komatireddy, R., Haaser, S., Topol, S., Sheard, J., Encinas, J., Fought, A.J., Topol, E.J., 2014. Comparison of 24-hour holter monitoring with 14-day novel adhesive patch electrocardiographic monitoring. *The American journal of medicine* 127, 95–e11.
- Blauw, H., Keith-Hynes, P., Koops, R., DeVries, J.H., 2016. A review of safety and design requirements of the artificial pancreas. *Annals of biomedical engineering* 44, 3158–3172.
- Bruttomesso, D., 2019. Toward automated insulin delivery.
- Caduff, A., Hirt, E., Feldman, Y., Ali, Z., Heinemann, L., 2003. First human experiments with a novel non-invasive, non-optical continuous glucose monitoring system. *Biosensors and Bioelectronics* 19, 209–217.
- Chen, L.Y., Tee, B.C.K., Chortos, A.L., Schwartz, G., Tse, V., J Lipomi, D., Wong, H.S.P., McConnell, M.V., Bao, Z., 2014. Continuous wireless pressure monitoring and mapping with ultra-small passive sensors for health monitoring and critical care. *Nature communications* 5, 1–10.
- Chen, Y., Lu, S., Zhang, S., Li, Y., Qu, Z., Chen, Y., Lu, B., Wang, X., Feng, X., 2017. Skin-like biosensor system via electrochemical channels for noninvasive blood glucose monitoring. *Science advances* 3, e1701629.
- Chen, Y.W., Periasamy, A.P., Chen, C.F., Chang, H.T., 2019. Quantification of glucose via in situ growth of cu2o/ag nanoparticles. *Sensors and Actuators B: Chemical* 285, 224–231. URL: <https://www.sciencedirect.com/science/article/pii/S0925400519300693>, doi:<https://doi.org/10.1016/j.snb.2019.01.050>.
- Choi, H., Naylon, J., Luzio, S., Beutler, J., Birchall, J., Martin, C., Porch, A., 2015. Design and in vitro interference test of microwave noninvasive blood glucose monitoring sensor. *IEEE transactions on microwave theory and techniques* 63, 3016–3025.
- Cobelli, C., Renard, E., Kovatchev, B., 2011. Artificial pancreas: past, present, future. *Diabetes* 60, 2672–2682.
- van Doorn, W.P., Foreman, Y.D., Schaper, N.C., Savelberg, H.H., Koster, A., van der Kallen, C.J., Wesselius, A., Schram, M.T., Henry, R.M., Dagnelie, P.C., et al., 2021. Machine learning-based glucose prediction with use of continuous glucose and physical activity monitoring data: The maastricht study. *PloS one* 16, e0253125.
- Ebrahimi, A., Coromina, J., Muñoz-Enano, J., Vélez, P., Scott, J., Ghorbani, K., Martín, F., 2021. Highly sensitive phase-variation dielectric constant sensor based on a capacitively-loaded slow-wave transmission line. *IEEE Transactions on Circuits and Systems I: Regular Papers* 68, 2787–2799.
- Farandos, N.M., Yetisen, A.K., Monteiro, M.J., Lowe, C.R., Yun, S.H., 2015. Contact lens sensors in ocular diagnostics. *Advanced healthcare materials* 4, 792–810.
- Gao, W., Emaminejad, S., Nyein, H.Y.Y., Challa, S., Chen, K., Peck, A., Fahad, H.M., Ota, H., Shiraki, H., Kiriya, D., et al., 2016. Fully integrated wearable sensor arrays for multiplexed in situ perspiration analysis. *Nature* 529, 509–514.
- Gecili, E., Huang, R., Khoury, J.C., King, E., Altaye, M., Bowers, K., Szczesniak, R.D., 2021. Functional data analysis and prediction tools for continuous glucose-monitoring studies. *Journal of clinical and translational science* 5.
- Gorst, A., Zavyalova, K., Mironchev, A., 2021. Non-invasive determination of glucose concentration using a near-field sensor. *Biosensors* 11, 62.
- Guliy, O., Zaitsev, B., Smirnov, A., Karavaeva, O., Borodina, I., 2019. Sensor for ampicillin based on a microwave electrodynamic resonator. *Biosensors and bioelectronics* 130, 95–102.
- Hanna, J., Bteich, M., Tawk, Y., Ramadan, A.H., Dia, B., Asadallah, F.A., Eid, A., Kanj, R., Costantine, J., Eid, A.A., 2020. Noninvasive, wearable, and tunable electromagnetic multisensing system for continuous glucose monitoring, mimicking vasculature anatomy. *Science Advances* 6, eaba5320.
- Hitzemann, M., Dehning, K.J., Gehl, A.V., Sterr, E.F., Zimmermann, S., 2022. Fast readout of split-ring resonators made simple and low-cost for application in hplc. *Electronics* 11, 1139.
- Jeong, S., Tentzeris, M.M., Kim, S., 2020. Machine learning approach for wirelessly powered rfid-based backscattering sensor system. *IEEE Journal of Radio Frequency Identification* 4, 186–194.
- Kazemi, N., Abdolrazzagh, M., Musilek, P., 2021a. Comparative analysis of machine learning techniques for temperature compensation in microwave sensors. *IEEE Transactions on Microwave Theory and Techniques* 69, 4223–4236.
- Kazemi, N., Musilek, P., 2022. Enhancing microwave sensor performance with ultrahigh q features using cyclegan. *IEEE Transactions on Microwave Theory and Techniques* 70, 5369–5382.
- Kazemi, N., Musilek, P., 2023. Resolution enhancement of microwave sensors using super-resolution generative adversarial network. *Expert Systems with Applications* 213, 119252.
- Kazemi, N., Schofield, K., Musilek, P., 2021b. A high-resolution reflective microwave planar sensor for sensing of vanadium electrolyte. *Sensors* 21, 3759.
- Keum, D.H., Kim, S.K., Koo, J., Lee, G.H., Jeon, C., Mok, J.W., Mun, B.H., Lee, K.J., Kamrani, E., Joo, C.K., et al., 2020. Wireless smart contact lens for diabetic diagnosis and therapy. *Science Advances* 6, eaba3252.
- Kim, J., Kim, M., Lee, M.S., Kim, K., Ji, S., Kim, Y.T., Park, J., Na, K., Bae, K.H., Kyun Kim, H., et al., 2017. Wearable smart sensor systems integrated on soft contact lenses for wireless ocular diagnostics. *Nature communications* 8, 1–8.
- Kim, J., Sempionatto, J.R., Imani, S., Hartel, M.C., Barfidokht, A., Tang, G., Campbell, A.S., Mercier, P.P., Wang, J., 2018. Simultaneous monitoring of sweat and interstitial fluid using a single wearable biosensor platform. *Advanced Science* 5, 1800880.
- Kim, N., Dhakal, R., Adhikari, K., Kim, E., Wang, C., 2015. A reusable robust radio frequency biosensor using microwave resonator by integrated passive device technology for quantitative detection of glucose level. *Biosensors and Bioelectronics* 67, 687–693.
- Kownacka, A.E., Vegelyte, D., Jooisse, M., Anton, N., Toebes, B.J., Lauko, J., Buzzacchera, I., Lipinska, K., Wilson, D.A., Geelhoed-Duijvestijn, N., et al., 2018. Clinical evidence for use of a noninvasive biosensor for tear glucose as an alternative to painful finger-prick for diabetes management utilizing a biopolymer coating. *Biomacromolecules* 19, 4504–4511.
- Lee, H., Choi, T.K., Lee, Y.B., Cho, H.R., Ghaffari, R., Wang, L., Choi, H.J., Chung, T.D., Lu, N., Hyeon, T., et al., 2016. A graphene-based electrochemical device with thermoresponsive microneedles for diabetes monitoring and therapy. *Nature nanotechnology* 11, 566–572.

- Lee, H., Song, C., Hong, Y.S., Kim, M.S., Cho, H.R., Kang, T., Shin, K., Choi, S.H., Hyeon, T., Kim, D.H., 2017. Wearable/disposable sweat-based glucose monitoring device with multistage transdermal drug delivery module. *Science advances* 3, e1601314.
- Lee, I., Probst, D., Klonoff, D., Sode, K., 2021. Continuous glucose monitoring systems-current status and future perspectives of the flagship technologies in biosensor research. *Biosensors and Bioelectronics* 181, 113054.
- Liao, Y.T., Yao, H., Lingley, A., Parviz, B., Otis, B.P., 2011. A 3- μ w cmos glucose sensor for wireless contact-lens tear glucose monitoring. *IEEE Journal of Solid-State Circuits* 47, 335–344.
- Martínez-Nieto, J.A., Medrano-Marqués, N., Sanz-Pascual, M.T., Calvo-López, B., 2019. High-level modeling and simulation tool for sensor conditioning circuit based on artificial neural networks. *Sensors* 19, 1814.
- Martinsson, J., Schliep, A., Eliasson, B., Mogren, O., 2020. Blood glucose prediction with variance estimation using recurrent neural networks. *Journal of Healthcare Informatics Research* 4, 1–18.
- Mohammadi, S., Nadaraja, A.V., Luckasavitch, K., Jain, M.C., Roberts, D.J., Zarifi, M.H., 2019. A label-free, non-intrusive, and rapid monitoring of bacterial growth on solid medium using microwave biosensor. *IEEE Transactions on Biomedical Circuits and Systems* 14, 2–11.
- Muckley, E.S., Lynch, J., Kumar, R., Sumpter, B., Ivanov, I.N., 2016. Pedot: Pss/qcm-based multimodal humidity and pressure sensor. *Sensors and Actuators B: Chemical* 236, 91–98.
- Nyein, H.Y.Y., Bariya, M., Tran, B., Ahn, C.H., Brown, B.J., Ji, W., Davis, N., Javey, A., 2021. A wearable patch for continuous analysis of thermoregulatory sweat at rest. *Nature communications* 12, 1–13.
- Omer, A.E., Shaker, G., Safavi-Naeini, S., Kokabi, H., Alquié, G., Deshours, F., Shubair, R.M., 2020. Low-cost portable microwave sensor for non-invasive monitoring of blood glucose level: Novel design utilizing a four-cell csr hexagonal configuration. *Scientific Reports* 10, 1–20.
- Pankratov, D., González-Arribas, E., Blum, Z., Shleev, S., 2016. Tear based bioelectronics. *Electroanalysis* 28, 1250–1266.
- Park, J., Kim, J., Kim, S.Y., Cheong, W.H., Jang, J., Park, Y.G., Na, K., Kim, Y.T., Heo, J.H., Lee, C.Y., et al., 2018. Soft, smart contact lenses with integrations of wireless circuits, glucose sensors, and displays. *Science advances* 4, eaap9841.
- Piekarz, I., Gorska, S., Odrobina, S., Drab, M., Wincza, K., Gamian, A., Gruszczyński, S., 2020. A microwave matrix sensor for multipoint label-free escherichia coli detection. *Biosensors and Bioelectronics* 147, 111784.
- Plaus, S., Schauer, S., Jendrike, N., Zschornack, E., Link, M., Hepp, K.D., Haug, C., Freckmann, G., 2021. Proof of concept for a new raman-based prototype for noninvasive glucose monitoring. *Journal of Diabetes Science and Technology* 15, 11–18.
- Pu, Z., Zhang, X., Yu, H., Tu, J., Chen, H., Liu, Y., Su, X., Wang, R., Zhang, L., Li, D., 2021. A thermal activated and differential self-calibrated flexible epidermal biomicrofluidic device for wearable accurate blood glucose monitoring. *Science Advances* 7, eabd0199.
- Rabby, M.F., Tu, Y., Hossen, M.I., Lee, I., Maida, A.S., Hei, X., 2021. Stacked lstm based deep recurrent neural network with kalman smoothing for blood glucose prediction. *BMC Medical Informatics and Decision Making* 21, 1–15.
- Rahmani, H., Archang, M.M., Jamali, B., Forghani, M., Ambrus, A.M., Ramalingam, D., Sun, Z., Scumpia, P.O., Coller, H.A., Babakhani, A., 2020. Towards a machine-learning-assisted dielectric sensing platform for point-of-care wound monitoring. *IEEE Sensors Letters* 4, 1–4.
- Rawat, K.A., Bhamore, J.R., Singhal, R.K., Kailasa, S.K., 2017. Microwave assisted synthesis of tyrosine protected gold nanoparticles for dual (colorimetric and fluorimetric) detection of spermine and spermidine in biological samples. *Biosensors and Bioelectronics* 88, 71–77.
- Rodbard, D., 2016. Continuous glucose monitoring: a review of successes, challenges, and opportunities. *Diabetes technology & therapeutics* 18, S2–3.
- Singh, A., 2017. Anomaly detection for temporal data using long short-term memory (lstm).
- Srichan, C., Srichan, W., Danvirutai, P., Ritsongmuang, C., Sharma, A., Anutrakulchai, S., 2022. Non-invasively accuracy enhanced blood glucose sensor using shallow dense neural networks with nir monitoring and medical features. *Scientific Reports* 12, 1–9.
- Wentholt, I.M., Hoekstra, J.B., DeVries, J.H., 2006. A critical appraisal of the continuous glucose-error grid analysis. *Diabetes Care* 29, 1805–1811.
- Wild, S., Roglic, G., Green, A., Sicree, R., King, H., 2004. Global Prevalence of Diabetes: Estimates for the year 2000 and projections for 2030. *Diabetes Care* 27, 1047–1053. URL: <https://doi.org/10.2337/diacare.27.5.1047>, doi:10.2337/diacare.27.5.1047, arXiv:<https://diabetesjournals.org/care/article-pdf/27/5/1047/566025/zdc00504001047.pdf>.
- Xiao, X., Yu, Q., Li, Q., Song, H., Kikkawa, T., 2020. Precise noninvasive estimation of glucose using uwb microwave with improved neural networks and hybrid optimization. *IEEE Transactions on Instrumentation and Measurement* 70, 1–10.
- Yilmaz, T., Foster, R., Hao, Y., 2014. Broadband tissue mimicking phantoms and a patch resonator for evaluating noninvasive monitoring of blood glucose levels. *IEEE transactions on Antennas and Propagation* 62, 3064–3075.
- Zheng, G., Patolsky, F., Cui, Y., Wang, W.U., Lieber, C.M., 2005. Multiplexed electrical detection of cancer markers with nanowire sensor arrays. *Nature biotechnology* 23, 1294–1301.
- Zou, Y., Chu, Z., Guo, J., Liu, S., Ma, X., Guo, J., 2023. Minimally invasive electrochemical continuous glucose monitoring sensors: Recent progress and perspective. *Biosensors and Bioelectronics* , 115103.